

Nanoscale

Accepted Manuscript

This article can be cited before page numbers have been issued, to do this please use: S. Najib, F. Bakan, N. Abdullayeva, R. Bahariqushchi, S. Kasap, G. Franzò, M. SANKIR, N. Demirci Sankir, S. Mirabella and E. Erdem, *Nanoscale*, 2020, DOI: 10.1039/D0NR03921G.



This is an Accepted Manuscript, which has been through the Royal Society of Chemistry peer review process and has been accepted for publication.

Accepted Manuscripts are published online shortly after acceptance, before technical editing, formatting and proof reading. Using this free service, authors can make their results available to the community, in citable form, before we publish the edited article. We will replace this Accepted Manuscript with the edited and formatted Advance Article as soon as it is available.

You can find more information about Accepted Manuscripts in the [Information for Authors](#).

Please note that technical editing may introduce minor changes to the text and/or graphics, which may alter content. The journal's standard [Terms & Conditions](#) and the [Ethical guidelines](#) still apply. In no event shall the Royal Society of Chemistry be held responsible for any errors or omissions in this Accepted Manuscript or any consequences arising from the use of any information it contains.

Tailoring morphology to control defect structures in ZnO electrodes for high-performance supercapacitor devices

Sumaiyah Najib¹, Feray Bakan², Nazrin Abdullayeva³, Rahim Bahariqushchi⁴, Sibel Kasap², Giorgia Franzo⁴, Mehmet Sankir^{3,5}, Nurdan Demirci Sankir^{3,5}, Salvo Mirabella^{4,6}, Emre Erdem^{1,2,*}

¹Faculty of Engineering and Natural Sciences, Sabanci University, 34956, Istanbul, Turkey

²Sabanci University SUNUM Nanotechnology Research Centre 34956 Istanbul, Turkey

³Micro and Nanotechnology Graduate Program, TOBB University of Economics and Technology, Sogutozu Cad. 43 Sogutozu, 06560, Ankara, Turkey

⁴IMM-CNR, via S. Sofia 64, 95123, Catania, Italy

⁵Department of Materials Science and Nanotechnology Engineering, TOBB University of Economics and Technology, Sogutozu Cad. No 43 Sogutozu, 06560, Ankara, Turkey

⁶Dipartimento di Fisica e Astronomia "Ettore Majorana", Università di Catania, via S. Sofia 64, 95123, Catania, Italy

Corresponding author email: emreerdem@sabanciuniv.edu

Abstract:

Zinc oxide (ZnO) nanostructures were synthesized in the form of nanoparticles, nanoflowers and nanourchins. Structural, electronic and optical characterization of the samples were done via standard techniques such as X-ray diffraction (XRD), scanning electron microscopy (SEM), photoluminescence, Raman and ultraviolet-visible (UV-Vis) spectroscopy. The point defect structures which are specific to each morphology has been investigated in terms of their concentration and location via state of art electron paramagnetic resonance (EPR) spectroscopy. According to core-shell model the samples all revealed core defects however the defects on the surface are smeared out. Finally, all three morphology has been tested as electrode material in a real supercapacitor device and the performance of the device, in particular, the specific capacitance and the storage mechanism has been mediated by the point defects. Morphology dependent defective ZnO electrode enable to monitor the working

principle of supercapacitor device from electric double layer capacitor (EDLC) to pseudo supercapacitor.

Article Online
DOI: 10.1039/D0NR03921G

1. Introduction

Nanostructured metal oxides, in particular, ZnO based morphologies, are promising electrode materials that can be used in energy harvesting and storage systems such as supercapacitors. The tunable bandgap, morphology, and size enable ZnO enormous applications in device technology [1,2]. The defective nature of ZnO causes difficulties to control the electronic and optical properties consequently at nanoscale due to the increasing concentration of surface defects control mechanisms to become more complicated [3–5]. Thanks to Electron Paramagnetic Resonance (EPR) and Photoluminescence (PL) techniques that obtained information enable one to identify, control, monitor, and tune the structural point defects [6]. The recently introduced core-shell model of ZnO nanoparticles at least distinguish very safely the defects located at the surface and the defects located at the core of ZnO [7]. According to the core-shell model, the surface defects more or less consist of delocalized conduction electrons and giving a g -factor at $g \sim 2.00$ and the core defects are localized having a g -factor of $g \sim 1.96$. Both defects can be due to ionized; oxygen vacancies (V_O), zinc vacancies (V_{Zn}), and interstitials. However, it is well known that the formation energy of oxygen vacancies is much lower than other defect vacancies therefore, ionized V_O are the more favorable defect centers both at the surface and the core but having different local environments. Thus the same kind of defect center gives different g -factor in the EPR experiment. Moreover, the shape, intensity, and isotropy of the individual EPR spectra for each defect center can be different which strongly depends on the morphology, spin density distribution, aspect ratio, and the dimension or size of the ZnO nanostructure [8]. Complementarily, PL spectra of defective ZnO has two distinct photoluminescent behavior which reveals representative PL peaks, one at ~ 380 nm (Near-Band-Edge (NBE) UV-emission) due to the bandgap of ZnO semiconductor crystal and the other one at ~ 630 nm (peak maximum) having broad visible light emission due to the structural defects. Here it is important to note, that in EPR only paramagnetically active defect centers give an EPR signal at $g \sim 2.00$ and 1.96, but in PL all defect centers may contribute to the defect-related PL emission at the visible light region. In this work, three different ZnO nanostructured morphologies were synthesized, their defect structures were thoroughly investigated and the roles of these defect structures that take effect on the electrochemical performance of hybrid supercapacitors were tested. Charge insertion and extraction ability of ZnO have been reported recently and highly promising specific capacitance values were reported [2]. Here one of the most important issues is to find out the most powerful synergy between the four components of the supercapacitor device namely ZnO electrode, carbon black electrode,

electrolyte (LiPF_6) and the separator (glass fiber). For sure novel designs by the aid of a proper selection of enhanced materials gives high prospects to the supercapacitor devices not only in high power density but also in high energy density. Thus this will allow it to become an alternative device to Li-ion batteries. Recently, we summarized all important aspects and current progress achieved in novel materials for supercapacitor electrodes in a mini-review [1]. Therefore, the materials' peculiarities are not visited here again. In this study, some of the important findings pertaining to ZnO on its novel growth morphology and related spectroscopic, optical, and electrochemical performance will be reported. Here, three different nanoarchitecture morphology of ZnO has been synthesized namely, nanoflowers, nanourchins, and nanoparticles. In particular, investigations of electronic properties via EPR, optical properties via Raman UV-Vis and PL and finally electrical properties via Cyclovoltammetry and Electrochemical Impedance Spectroscopy (EIS) enabled us to extensively control the defects in these various morphologies. Hence, qualitative relationship between process morphology, defects and electrochemical performance of the electrode material has been achieved and discussed in a very compact way. Comparative study of nanoflowers, nanourchins, and nanoparticles as an electrode gave us a reliable electrochemical performance results while we keep the electrolyte, separator and the second electrode always the same for each device. Such supercapacitor devices will be the basis for a prototype model for the battery-type energy saver metal oxide based supercapacitors which can be used in future electrical vehicles [9] or solar systems of micro satellites [10].

2. Experimental

2.1 Fabrication of ZnO Nanostructures

Nanoparticles (NP) and Nanourchins (NU): Fabrication of ZnO NPs have been performed via a hydrothermal process in a solution containing 0.05 M zinc acetate dihydrate ($\text{Zn}(\text{C}_4\text{H}_6\text{O}_4 \cdot 2\text{H}_2\text{O})$) as the zinc source and 1.0 M urea as the precursor. The pH value of the solution has been adjusted to precisely 4.8 with the acetic acid (CH_3COOH). For the ZnO NU synthesis, the hydrothermal step has been carried out by using zinc nitrate hexahydrate ($\text{Zn}(\text{NO}_3)_2 \cdot 6\text{H}_2\text{O}$) and urea of the same molarities. At this step, the pH adjustment has been conducted via dilute nitric acid and the pH value has been set to 4.5 strictly. Both of the prepared solutions have been kept in the oven at 80 °C for 3 h. The composed ZnO powders have been further filtered and washed several times to discard contaminations and dried in calcination oven at 300 °C for 30 min. at ambient air. All chemicals have been purchased from Sigma-Aldrich and have been used without further purification.

Nanoflowers (NF): The synthesis process for one-dimensional ZnO NFs have also been conducted via the hydrothermal method in an aqueous solution containing 0.1 M zinc nitrate hexahydrate ($\text{Zn}(\text{NO}_3)_2 \cdot 6\text{H}_2\text{O}$) and aqueous ammonium hydroxide solution (2% v/v). The

reaction process has been kept for 1 h at 80 °C, and the formed powders have been washed and filtered for the proceeding annealing step conducted at 300 °C for 30 min. at ambient air. Here also, the chemicals have been purchased from Sigma-Aldrich and have been used without further purification.

ZnO nanostructure formation process indeed can be divided into two main reaction steps which are (I) nucleation and (II) growth [11]. For the initiation of the primary nucleation step the supersaturation of the prepared ZnO solution should take place. This step is highly dependent on the solubility of the precursor material, which in the case of NP and NU is urea that has slow and gradual hydrolysis kinetics in water [12]. This results in the realization of the following reaction steps that eventuate with the release of carbon dioxide and hydroxide ions into the reaction media:



It is highly essential to point out that the slow dissociation of urea causes a constant increase in the pH value of the solution during the 3 h reaction period. During this period, the reaction should not exceed the pH value of 9.0 for the successful precipitation to occur. Therefore, the arrangement of pH value prior to the reaction initiation is a crucial step for ZnO nanopowder synthesis. Moreover, the acidic pH adjustment of both NP and NU solutions results in the preferential transformation of carbonate ions into zinc carbonate hydroxide hydrate ($\text{Zn}_4\text{CO}_3(\text{OH})_6 \cdot \text{H}_2\text{O}$) with heterogeneous nucleation sites providing various 3D nanostructure growth. Hereupon, the resulting nanostructure starts to depend only on the anionic source. $\text{Zn}(\text{C}_4\text{H}_6\text{O}_4 \cdot 2\text{H}_2\text{O})$ standing for the anion source of NP structures has a tendency to be incorporated into the growing crystal during the reaction, while $\text{Zn}(\text{NO}_3)_2 \cdot 6\text{H}_2\text{O}$ initiating the NU growth is featured as a non-complexing weak base. This type of anion is mostly adsorbed on the foretime grown crystal structure [12]. On the other hand, NF growth mechanism, due to its one-dimensional (1D) orientation, varies from those of NU and NP. Ammonium hydroxide is selected as the precursor material providing both the OH^- and NH_4^+ ions which serve as the oxygen source in ZnO and provide a buffering mechanism to form complexes with Zn ions [13]. The formation of complex hydroxyl species as a result of OH^- and Zn^{2+} initiates the nucleation step. Further control over the growth kinetics and mechanism is provided through ammonia ions, facilitating specific coordination which varies with the reaction parameters such as reaction temperature, solution concentration, and growth period [14].

2.2 Methods

View Article Online
DOI: 10.1039/D0NR03921G

Raman Spectroscopy measurements were performed using a Renishaw Raman InVia System coupled with a 532 nm green laser having random photon polarization. The as-synthesized materials were characterized by Raman (Renishaw inVia Reflex). Raman data were collected using a 532 nm laser source with 2 μm spot size within the range of 100-3000 cm^{-1} in order to identify the nanoparticles. The UV transition and visible emission band for all the samples were measured using Photoluminescence (PL) spectroscopy at room temperature. PL measurements were performed by pumping with the 325 nm (3.82 eV) line of a He-Cd laser chopped through an acoustooptic modulator at a frequency of 55 Hz and a fixed power of 1.5 mW. The PL signal was analyzed by a single grating monochromator, detected with a Hamamatsu visible photomultiplier, and recorded with a lock-in amplifier using the acoustooptic modulator frequency as a reference. Electron Paramagnetic Resonance (EPR) measurements were performed with a Bruker Benchtop EMX Nano EPR spectrometer with an integrated referencing for g -factor calculation and also integrated spin counting unit. The microwave frequency of the resonator was 9.41 GHz and all spectra were measured with 5 mW microwave power at room temperature. Electrical impedance spectroscopy (EIS) measurements were carried out using a Versastat IV potentiostat (Princeton Applied Research) in atmospheric pressure at room temperature in the frequency range between 0.1 Hz and 100 kHz. For analyzing the spectra we used the Versa Studio V2.4 software. The amplitude of voltage modulation was set to 100 mV. For all supercapacitors, cyclic voltammetry (CV) was performed in voltage ranges of -1 V to 1 V for the cells with LiPF_6 electrolyte with the voltage sweeping rate of 0.01 Vs^{-1} . In the present case, a four-point electrode-setup was used to measure the real supercapacitor devices.

2.3 Electrodes and supercapacitor device design

ZnO and carbon black materials were used as electrodes without any additives such as polymeric binders or carbon materials. This means there is no slurry phase in the present supercapacitor design. In order to test the performance of ZnO and dependency of morphology and defect centers only asymmetric supercapacitor was designed being one electrode ZnO and the other one is carbon black. WHA1825042-Whatman® glass microfiber filters, Grade GF/F, were used as the dielectric separator; these filters are highly porous and effective to separate the two electrodes. Finally, well-known 1 M LiPF_6 (lithium hexafluorophosphate) dissolved in 50/50 (v/v) mixture of ethylene carbonate and diethyl carbonate EC/DMC (Aldrich) electrolyte was used to get a wide range of voltage window. The full cell supercapacitors with LiPF_6 as the electrolyte were assembled in a glove box filled with Ar ($[\text{O}_2] < 0.5 \text{ ppm}$). The full cell design is illustrated in Fig. 1. These designs were successfully implemented in former studies based on superbat [2],

octacalcium phosphate [15], carbon dots [16,17], and high energy ball milled ZnO/graphene foam [18] electrodes.

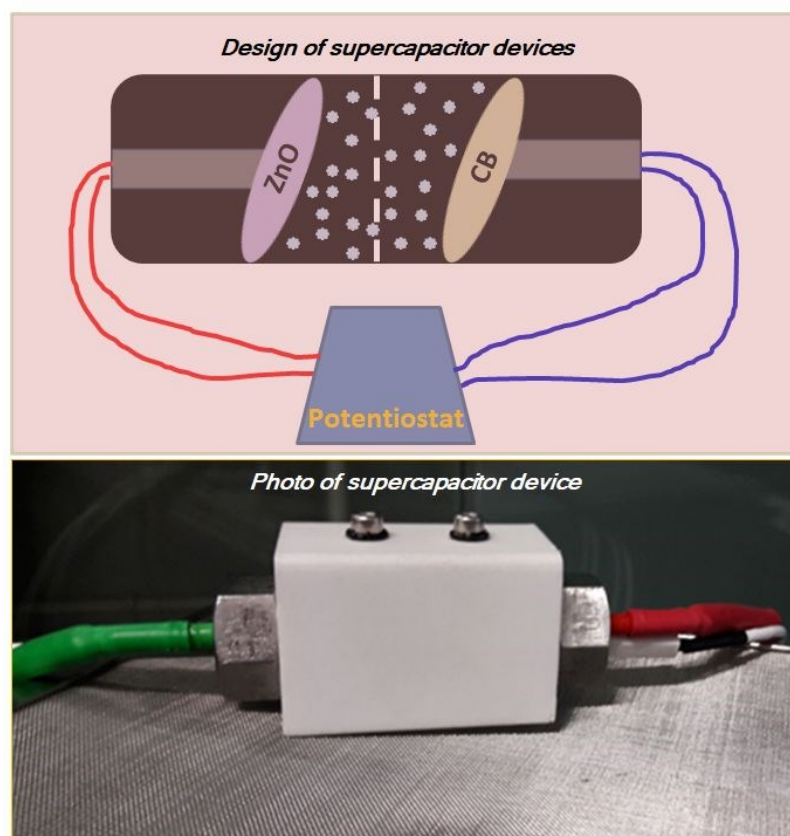


Figure 1: The *top* part of the figure shows the schematic for the asymmetric supercapacitor design. The photograph at the *bottom* displays the actual setup built during the experiment.

3. Results and Discussion

X-Ray Diffraction (XRD) spectra in Fig. 2a obtained from ZnO NP, NU, and NF powders represent hexagonal wurtzite crystal structure formation [19]. The characteristic peaks obtained at (100), (002) and (101) diffraction patterns have relatively proximate intensities with a significant shift in NFs compared to the other two nanostructures. It is important to note that NFs as thin films are 1D nanostructures with unidirectional (c-axis) orientation. However, as evidenced by SEM images NF structures gather to form a bunch, thus losing their 1D preference. Therefore, the (002) diffraction peak at $\sim 34.72^\circ$ is not as strong as it is expected to be in common NF thin films [20,21]. Another important parameter to be discussed is the obvious shift observed in XRD patterns of NFs. The position of the diffraction peak is useful for the detection of lattice planes and their locations within the

crystal structure. An approximate shift of 0.3° towards a higher X-ray angle has been detected which might be caused by several reasons. The most common rationale lying behind the peak shift is due to the change in the stress of ZnO nanostructures [22]. Two main causes of stress have been previously reported in the literature of which are; (i) the intrinsic stress caused by defects and impurities located in the crystal structure and, (ii) the extrinsic stress resulting from growth conditions and lattice mismatch [14,22]. Lattice disorders, oxygen vacancies, and zinc interstitials are among several defects that can be listed for ZnO nanostructures causing stress within the crystal structure. According to Bragg's law, wurtzite peaks of NFs that appear at higher diffraction angles can be correlated with smaller lattice spacing within the nanostructure. The decrease in the corresponding lattice spacing can be correlated with the oxygen vacant regions bringing about X-ray peak shifts towards higher diffraction angles [14]. Similarly, the presence of zinc interstitial in NP and NU structures may result in larger lattice spacing, thus shifting the wurtzite diffraction peaks of NP and NU towards lower 2θ values. Combining these indications with the conducted EPR and PL analyses (will be given below), it can be concluded that the variations in the defect densities and feature sizes of all three nanostructures have an ultimate impact on the resulting XRD spectra. Fig. 2(b-d) is the SEM results of the ZnO samples showing the nanoflower, nanourchine and nanoparticle morphology. Here the morphologies distinctly distinguishable from each other. Here one may not easily speak about the dimension because of the undefined dimension of flowers or urchins via SEM. Nevertheless all structures are showing nanoscale dimensions having reasonable homogeneity. Energy dispersive x-ray (EDX) spectra in Fig. 3 revealed correct stoichiometry and correct atomic ratio in terms of ZnO crystal structure.

Manuscript Online
DOI: 10.1039/D0NR03921G

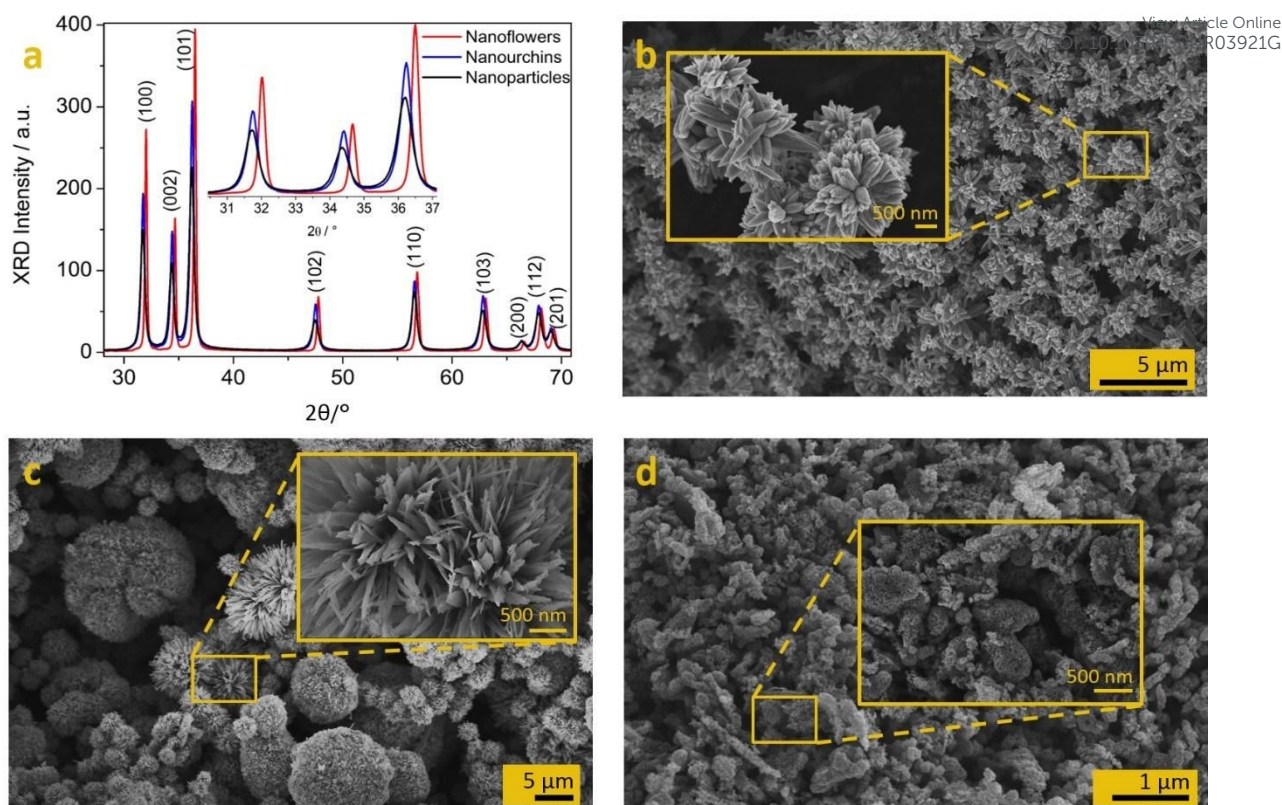


Figure 2: Structural and morphological investigation of different ZnO nanostructures. **a)** Powder X-ray diffraction patterns of ZnO nanostructures. All the indexed peaks in the obtained spectra are matched with the planes of the ZnO hexagonal wurtzite structure (01-079-0207). **b)** Secondary-electron SEM micrograph of ZnO nanoflowers, **c)** Secondary-electron SEM micrograph of ZnO nanourchins, and **d)** Secondary-electron SEM micrograph of ZnO nanoparticles. All images were recorded through an in-lens detector with an accelerating voltage of 5 keV. In the inset, higher magnification of each image is given.

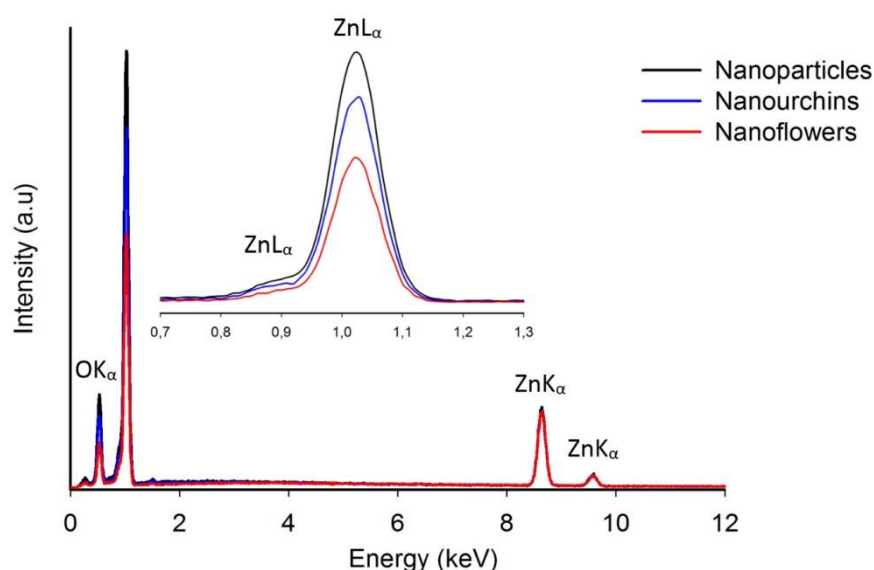


Figure 3: EDX spectra of three different ZnO nanostructures. The analyses were conducted at 18 keV accelerating voltage.

Raman spectroscopy enabled differentiating the phase variants and if exist the defect density related vibration modes of ZnO nanostructures at the molecular level. ZnO crystallizes as hexagonal wurtzite which belongs to the C_{6v}^4 ($P6_3mc$) space group and the only optical phonons at Γ point of the Brillouin zone give rise to a first-order Raman scattering [20,23,24]. The predicted zone-center optical modes are A_1 , $2B_1$, E_1 , and $2E_2$ where B modes are silent [24,25]. In the wurtzite structure, each Zn ion is surrounded by the tetrahedron of oxygen ions and vice versa and this orientation leads to polar symmetry along the hexagonal vertical axis (c axis) which results in A_1 and B_1 mode oscillations [23]. On the other hand, when the atom displacement is perpendicular to the c-axis the twofold degenerate E modes occur. The E_1 mode exhibits an oscillating polarization while the E_2 modes that consist of $E_2(\text{low})$ and $E_2(\text{high})$ are non-polar. The $E_2(\text{low})$ mode is mainly associated with the vibration of the Zn sublattice, while the $E_2(\text{high})$ mode mainly comes from the vibration of the O sublattice [23,25]. The polarity induces a splitting of the A_1 and E_1 modes into transverse optical (TO) and longitudinal-optical (LO) phonons.

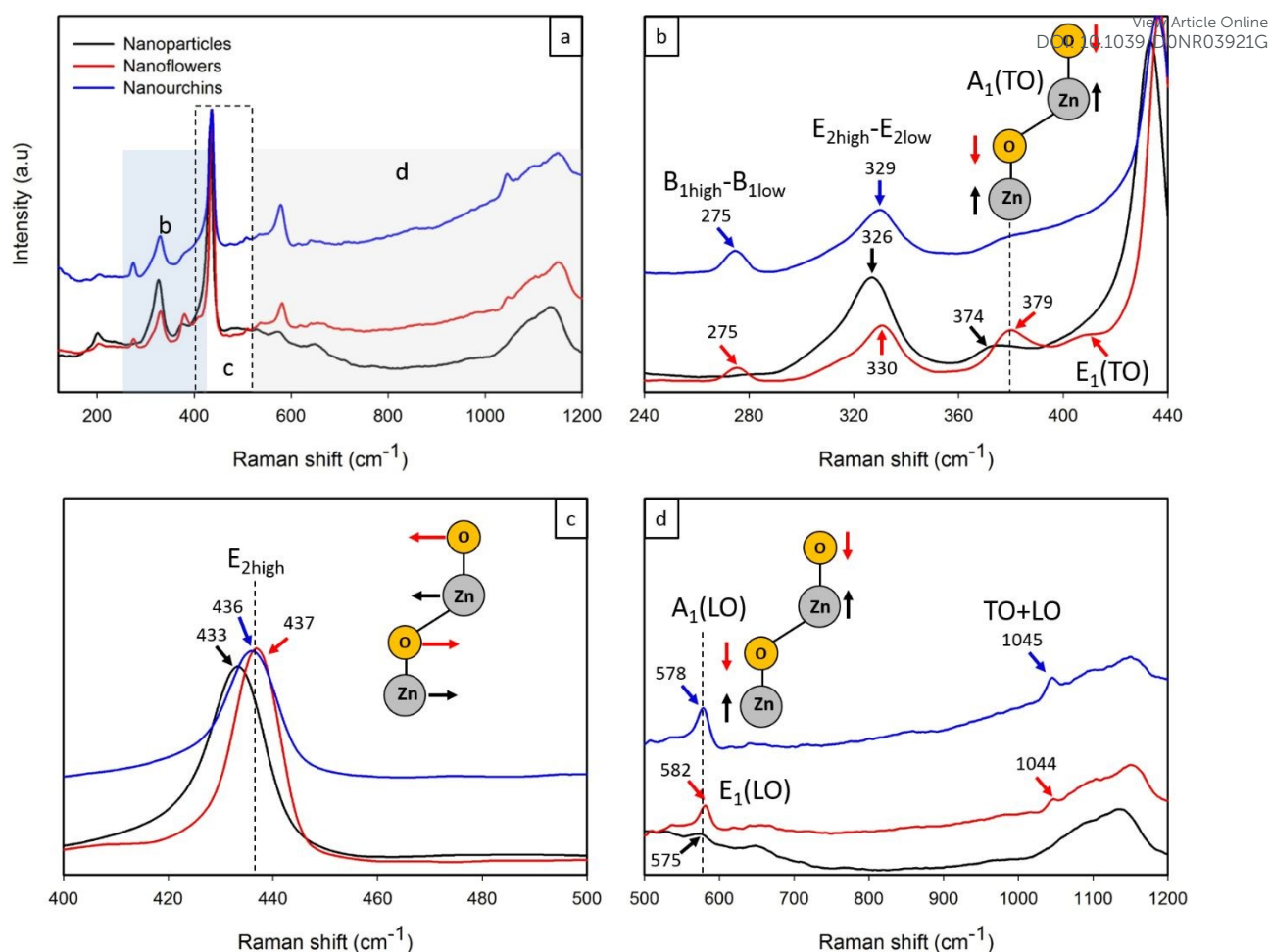


Figure 4. First-order and second-order Raman spectra of three different ZnO nanostructures ($\lambda=532$ nm). The regions designated as b, c and in Fig. (a) are extended in Figs. (b, c and d).

The Raman spectra of three different ZnO nanostructures are given in Fig. 4 (a-d) to reveal the differences as a function of different morphologies. Owing to the strong occurrence of E_2 modes in standard backscattering experiments, these modes are considered to be a Raman fingerprint for ZnO. In Fig. 4c, a strong peak at around 436 cm^{-1} is assigned to the characteristic Wurtzite $E_{2\text{high}}$ mode of ZnO. This peak is shifted to lower wavelengths in the case of NPs. Such an occurrence may be due to anisotropic internal strains corresponding to different growth directions, the defects or impurities in the nanocrystal, laser irradiation-induced heating or optical phonon confinement in different nanostructures. As the dimensions of nanostructures are bigger than the Bohr exciton radii (≈ 2.34 nm), the optical phonon confinement is possible but should not be expected to be the only mechanism [25]. The possible effect of laser irradiation on the vibrational modes was tested by applying various laser powers. No apparent band shift or broadening was observed, allowing us to carry out the rest of the experiments at 100% laser power in the static scan. The $E_{2\text{low}}$ mode

could not be detected for all three nanostructures (Fig. 4a). However, the vibration at around 330 cm^{-1} is generally attributed to the second-order Raman process and assigned to the $E_{2(\text{high})}-E_{2(\text{low})}$ difference mode. This assignment was recently confirmed by both symmetry considerations and temperature-dependent intensity analysis [23,26]. Therefore, it can be concluded that the $E_{2\text{low}}$ band may exist as broadband with low intensity. It should be considered that in the case of the second-order Raman process, predominant combination bands are present which belongs to the total frequencies of optical branches. This can be attributed to the possible surface and/or aggregate defects in the structure. This is also another indication for the existence of the structural defects which should be correlated to the EPR results. When the incident and scattered light are perpendicular to the c-axis, TO modes are allowed and the related Raman bands are given in Fig. 4b. $A_1(\text{TO})$ and $E_1(\text{TO})$ modes were not observed for the NUs. In the case of NFs, the obvious peak at 379 cm^{-1} is attributed to $A_1(\text{TO})$ mode, while the weak shoulder peak at 408 cm^{-1} is assigned to $E_1(\text{TO})$ mode. For NPs, only $A_1(\text{TO})$ mode was observed at 374 cm^{-1} . The $A_1(\text{LO})$ phonon mode can appear only when the c-axis of wurtzite ZnO is parallel to the sample surface. The weak peak at around 575 cm^{-1} and the more intense peak at 578 cm^{-1} can be attributed to the $A_1(\text{LO})$ modes in the ZnO NPs and NUs, respectively. When the c-axis of wurtzite ZnO is perpendicular to the sample surface, the $E_1(\text{LO})$ phonon is observed at 582 cm^{-1} in the case of NF (Fig. 4d). In the high-frequency range, the most significant second-order features correspond to LO overtones and the combinations of LO modes [26]. In Fig. 4d, the broad bands in between $1030\text{--}1200\text{ cm}^{-1}$ should belong to the multiphonon process. The broad peak at around 1150 cm^{-1} may correspond to 2LO scattering from flat bands along the A-L-M line, possibly in combination with the modes $2A_1(\text{LO})$ and $2E_1(\text{LO})$ inside of the first Brillouin zone [26]. This band was observed at 1135 cm^{-1} in the case of NPs. The weak shoulders at around 1044 cm^{-1} can be attributed to the TO+LO combinations at the A and H points of the NFs and NUs, whereas this multiphonon band could not be observed for the NPs.

Table 1. Room temperature frequencies and symmetries of the first- and second-order Raman spectra observed in different ZnO nanostructures. Parentheses indicate symmetries that although being present in the spectra display a much lower intensity than the dominant one.

Symmetry	Process	Nanoparticles	Nanoflowers	Nanourchins
		Raman shift (cm ⁻¹)		
A ₁ , E ₂	*2TA; 2E _{2low}	201	203	204
A ₁	B _{1high} - B _{1low}	-	275	275
A ₁ , (E ₂ , E ₁)	E _{2high} - E _{2low}	326	330	329
A ₁	A ₁ (TO)	374	379	-
E ₁	E ₁ (TO)	-	408	-
E ₂	E _{2high}	433	437	436
A ₁	A ₁ (LO)	575	-	578
E ₁	E ₁ (LO)	-	581	-
A ₁	**TO+LO	-	1044	1045
A ₁	***2A ₁ (LO), 2E ₁ (LO); 2LO	1135	1154	1151

*L, M, H ;Γ Brillouin zone points/lines [23,26], **A,H Brillouin zone points/lines [23,26], *** Γ; A-L-M Brillouin zone points/lines [23,26].

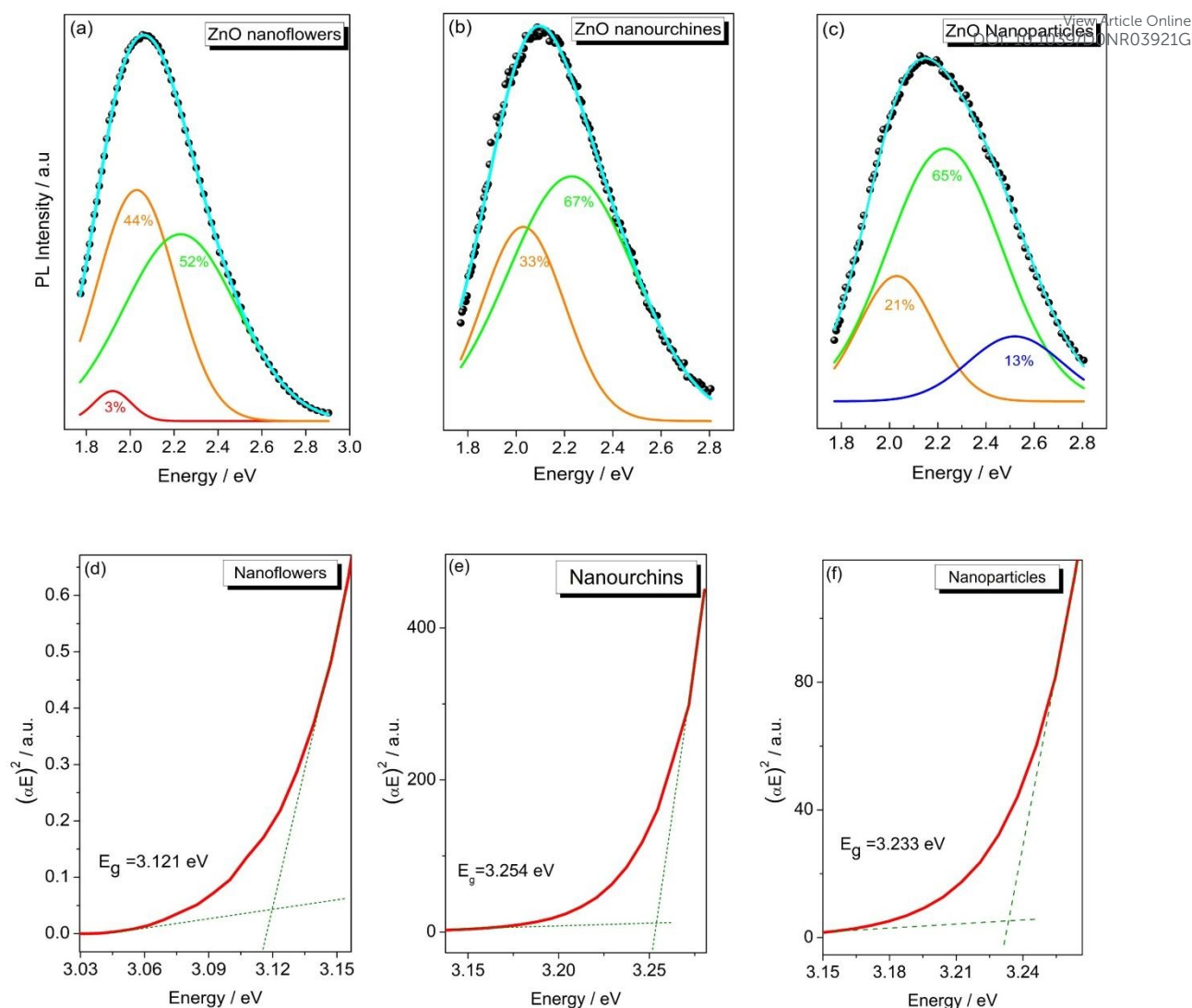


Figure 5: The PL intensity versus energy graphs (a-c) and Tauc-plots (d-f) obtained from UV-Vis reflectance spectra for the different ZnO nanostructures.

In Fig. 5 (a-c) it is observed, three PL spectra for different morphologies of ZnO. Defect related PL spectra originate from all kinds of defects in ZnO and the green emission is mostly responsible for the V_o . Unlike PL, EPR spectroscopy is only sensitive to paramagnetic defects but by the aid of EPR, it is possible to distinguish surface and core defects due to the g -factor difference. Namely, the point defects located at the surface give $g \sim 2$ and at the core gives ~ 1.96 [7]. Therefore it is crucial to determine defect art from PL and their location form EPR [5]. According to PL, blue (13% for NF), green (65%, 67% and 52% for NPs, NUs, and NF, respectively) orange (33% and 44% for NU and NF) and finally red emission (3%) is related to Zn vacancies (V_{Zn}) at the surface, singly ionized oxygen vacancies (V_o^+) at the surface, oxygen vacancies (V_o) at the core and to the interstitial oxygen vacancies (O_i) located at the surface respectively [27]. From these results, we confirm that the defect structures are strongly dependent on the morphology. There is a strong tendency of redshift

in NF even red emission is observed indicating O_i-defects. From the EPR point of view, all paramagnetically active defect centers have been already listed in a very detailed way in our previous works [4,5,7]. The bandgap energy of the various morphologies of ZnO samples were measured by the use of reflection spectra that were performed via UV-Vis spectroscopy. For determining the bandgap experimentally, the absorption coefficient α is deduced from the following equation, where R_{\max} is the value of the maximum reflectance, R_{\min} is the value of the minimum reflectance and R is the reflectance values.

$$\alpha = \ln \left[\frac{R_{\max} - R_{\min}}{R - R_{\min}} \right] \quad (3)$$

Then in this approximated technique typically a curve between $(\alpha hu)^2$ versus photon energy (hu) is plotted. The intercept of this plot on the energy axis is defined as the bandgap of ZnO nanocrystals. This procedure is commonly used for determining the bandgap energy of semiconductors [28,29]. By the examination of bandgap energies by UV-Vis spectroscopy following bandgap energy (E_g) values was obtained by the aid of Tauc-plot as presented in Fig. 5 (d-f): 3.233 eV, 3.121 eV, and 3.254 eV for nanoparticles, nanoflowers and nanourchins, respectively. Certainly, this method gives approximately the accurate estimation of bandgap however it may not be reliable enough to correlate the E_g values with defect concentration or any other physical parameters such as conductivity, capacitance, or g-factor.

The EPR Fig. 6a, shows two distinct EPR signal at $g= 2.002$ and $g=1.962$. As previously discussed, the signal at $g= 2.002$ is arising from the defect centers in ZnO located at the surface and $g= 1.962$ signal is arising from the defects located at the core of the ZnO. Here, in combination with PL we not only have tested the morphology dependence of defect centers in ZnO but also their concentration dependency by the aid of spin counting procedure [3,30] Thanks to spin counting method that one may obtain accurately the concentration of paramagnetic defect centers by simply double integrating the first derivative of EPR signal. Comparing the area of the integrated EPR signal with the standard sample with known spin concentration gives the defect concentration. Moreover, by the aid of EPR it is possible to determine the saturation behavior of the defect centers which give rise to EPR signal meaning that the ones which are paramagnetic. Microwave saturation data, in general, give information on the trap electrons whether they are bounded or unbounded. Further one may obtain information about the spin-lattice relaxation time [5,31]. As it is seen from Fig. 6a, all three nano-morphology (particles, urchin, and flower) have core signals. On the other hand, the EPR intensity of shell signal hence the concentration of surface defects is strongly dependent on the morphology. From the extended figures, it is seen that NUs have

decreased concentration of surface defects. NPs have the highest amount of defects compared to NF and NU. It is known that the conduction electrons saturate easily [3–5,7], whereas the bound-state electrons saturate with much more difficulty with respect to the square root of microwave power. Therefore according to our past research on defects in the frame of the core-shell model that one expects easy saturation for surface defects and hard or almost no saturation for core defects. This has been already proved by the investigation of various ZnO monocrystalline samples [3–5] and also for carbon materials such as C-dots [17]. In present work, we realized that the defect structure thus the behavior of them under microwave power is completely different and quite complicated. Since the EPR signal of surface defects around $g \sim 2$ is too weak so that we cannot perform reliable power dependency on this signal for all three samples. Based on the power dependency of the core defects at $g \sim 1.96$ we may say that the nanoparticles follow the expectation of the core-shell model where there is no saturation in the EPR intensity. However, according to electrical results (will be given below), this sample has the highest conductivity. That means the defect type change from V_o to either V_{Zn} or O_i . While in ZnO particles the major defect center is expected to be the V_o due to their lower formation energy. Thus, here the situation changed and this is most probably based on the synthesis route. As listed in Table 2, in the case of nanoflowers and nanourchins strong saturation behavior is observed at 15.23 and 12.56 mW, respectively. This means the core defects are acting as surface defects. This sounds strange however the morphology of the ZnO changed the electronic environment thereby the local configuration and the saturated core defects are revealed, unexpectedly. This also means that morphology dependent defect centers may drastically alter the spin-lattice relaxation times.

Article Online
DOI: 10.1039/D0NR03921G

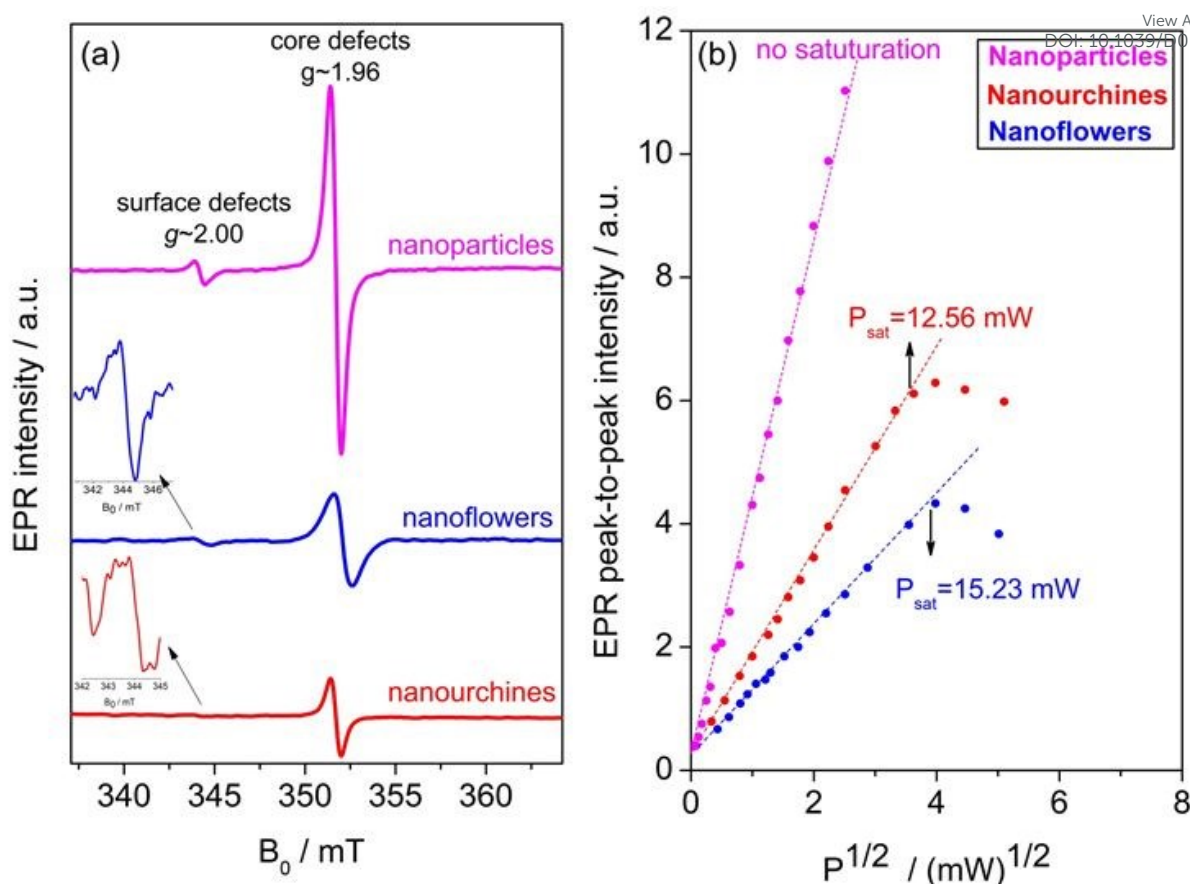


Figure 6: (a) Intensity measured at room temperature X band (9.47Hz) EPR and (b) plot of EPR peak to peak intensity with respect to $P^{1/2}$ for the hydrothermal processed three different nanostructures of ZnO.

Table 2: Different recorded parameters for core and shell of the various ZnO nanostructures.

	g-factor	Defect concentration (spins/mg)	Power saturation (mW)
Nanoparticles			
core	1.9591(5)	2.23×10^{13}	No saturation
shell	2.0027(5)	7.65×10^{11}	-
Nanoflowers			
core	1.9580(5)	3.56×10^{12}	15.23
shell	2.0024(5)	2.45×10^{11}	-
Nanourchins			
core	1.9597(5)	0.56×10^{12}	12.56
shell	2.0034(5)	0.12×10^{11}	-

It is well known that electric double layer capacitor (EDLC) stores the energy through Helmholtz double layer process whereas the pseudocapacitors give a high specific capacitance due to the Faradaic reversible redox charge storage mechanism [32]. The best way to test whether the storage system of a capacitor behaves as EDLC or faradaic is to perform impedance and cyclovoltammograms measurements. The well-known Nyquist plots were

presented in Fig 7a. Normally, ZnO material shows resistance values in the order of Giga Ohm [3], here due to the synergy of ZnO, electrolyte, and the carbon black the supercapacitor revealed resistance values in order of approx. 50-1000 Ohm depending on the morphology of the ZnO material. In Nyquist data, the first semicircle is responsible for the charge transfer resistance R_{ct} which is the lowest for nanoparticles (less than 100 Ω). Compared to nanoparticles the nanoflowers and nanourchines which are less defective than the nanoparticles revealed higher R_{ct} . It is worth mentioning that faradaic storage mechanisms, in general, show higher conductivity which also confirmed here by Nyquist in the case of nanoparticles. This is quite good agreement with the EPR microwave power saturation data as well which is presented in Fig. 6b. On the other hand, nanourchines show some traces of the ideal supercapacitor due to the non-existing first semicircle. Thus, for less defective samples the CV curve should give curves like rectangular shape and the nanoparticles which are almost Faradaic should reveal deviated rectangular form by humps. This has been tested via potentiostat and results are presented in Fig 7b. CV plots for each device based on morphologically different ZnO electrodes display quasi-rectangular shapes, the CV curves became leaf-like and mirror-symmetric in shape. The curves are indicating modest ideal supercapacitive properties and outstanding reversibility of the electrodes. Each device has an almost similar nature which indicates that each device can perform within potential window -1 to 1 V without any degradation. This result also indicates the dominance of the electrical double layer mechanism in the energy storage process. Normally, when ZnO is used as highly defective material as the electrode, then the pseudocapacitance behavior is expected. This has been confirmed by our previous supercapacitor studies as well.

Article Online
DOI: 10.1039/D0NR03921G

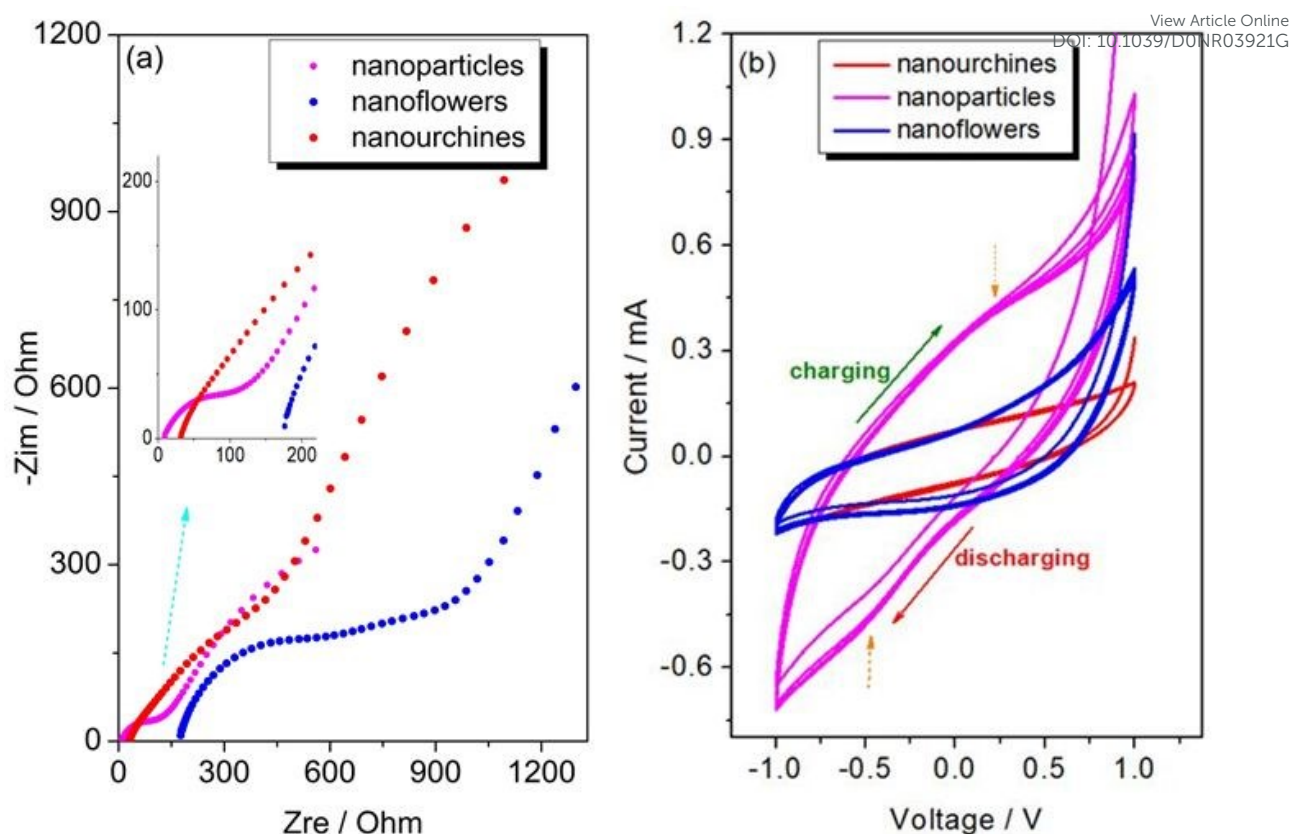


Figure 7: The electrochemical behavior of three produced supercapacitors investigated by a) EIS in Nyquist plot of the supercapacitors, and b) behavior of charge-discharge (intercalation-deintercalation) via the cyclic voltammetry (CV).

From the point of defect, concentrations compare to other synthesis techniques present synthesis route revealed several orders of less defect centers in all morphologies compared to superbats [2], or high energy ball milled ZnO nanocrystals [18]. From the EPR spin counting data, this has been confirmed and given in Table 2. In particular, the decrease in surface defects from nanoparticles, nanoflowers, and nanourchines, respectively can be correlated to not only capacitive behavior but also storage mechanism. Nevertheless, CV curve of nanoparticles given in Fig. 7b has slightly deviated from the quasi-rectangular shape and showed small humps indicating Faradaic reaction. The orange dashed arrows indicate the humps for eyes in the Fig. 7b. That means in case nanoparticles has sufficient amount of defect centers both on bulk and surface such bumps will be rising and create extra room for charges to give high capacitance values. Such a result, compare to other highly defective ZnO electrodes, shows that the morphology thus the concentration, and the synthesis route are playing crucial role for the capacitive performance of the supercapacitor devices. More than this, the defect concentration determines the working principle of the device whether it is EDLC or pseudocapacitance. Therefore, by defect mediated supercapacitors it may be possible to control the energy storage mechanism. Further, The gravimetric ($C, F \cdot g^{-1}$) specific

capacitance can be obtained from these CV curves at certain current density based on the following equation: $C = I / m (\Delta V / \Delta t)$ where I (A) is the discharge current, Δt (s) is the discharge time, m (g) is the mass of active materials (the areal density of ZnO and carbon black on the electrode is ca. 20 mg·cm⁻²) and ΔV (V) is the operation discharge voltage window. Finally, the calculated specific capacitance values are 330 F/g, 177 F/g, and 66 F/g at 0.1 C current density for nanoparticles, nanoflowers, and nanourchines, respectively. These capacitance values are lower than the pseudocapacitive superbat device which is based on a highly defective ZnO electrode that is yielding 448 F/g specific capacitance. The decrease in capacitance can be associated to the low utilization of electroactive materials at lower defect concentrations since the limited amount of electrolyte ions can enter into the inner structure and outer active surface of the active material. In the case of defective ZnO the scenario is much different. Due to the high amount of defect concentration blocking mechanisms of electron transport occurs at the interfaces and organizes as a double layer and contribute to the capacitance. These make extra room (like a camel-hump) for point charges and increase the capacitive behavior. In other words; the number of mobile defects transporting absorbed within the medium could be higher with enhanced mobility which helps in improving the charge storage capacitive behavior. Lower defect concentration blocks the ion migration within the electrolyte and diminishes the charge accumulation at the electrolyte-electrode interface. Therefore, fewer defects are drifted from an electrode to another electrode and hence less absorbed onto the active electrode forming charge accumulation at the electrode-electrolyte region.

4. Conclusions

Various types of ZnO nanoscaled morphologies were synthesized successfully and characterized by the XRD, SEM, and EDX from the structural point of view. Point defects for each morphology have been identified and quantitatively analyzed via Raman, PL and in particular with EPR. The detailed EPR analysis such as spin counting and microwave power saturation revealed extensive information on the local electronic environment, concentration, and location of the defect centers. According to the results, the defect centers play a central role for defect-related emission which arise from all defects exists in the ZnO sample. On the other hand, paramagnetic defects mostly singly or doubly ionized vacancies or interstitials can only be detected via EPR spectroscopy solely. The surface ($g \sim 2.00$) and core ($g \sim 1.96$) defects can be separated safely due to their g -factor and here NP, NF, and NU samples compared to other nanostructured samples in literature the surface defect concentration is too less. Moreover, in these specific samples, the defects on the core do not properly follow the core-shell model. The defect centers behave like a surface defect indicating conductive

behavior. This can only be explained by the character of the synthesis technique and the morphology. The core-shell model has been proposed by the well-defined hexagonal nanocrystals whereas here we have quite different structures having an undefined aspect ratio. Real supercapacitor devices assembled for understanding the capacitive behavior of ZnO nano-morphologies. Specific capacitance values are promising and deviated from ~330 to 65 F/g at 0.1 C depending on the morphology of ZnO. Here the synergy of the ZnO with the electrolyte and the counter electrode carbon black played a vital role in the electrochemical performance. Normally defective metal oxides reveal Faradaic storage mechanism once they are used as an electrode in supercapacitors. Surprisingly, we obtained EDLC character in the supercapacitor devices in particular for the less defective nanourchine samples. When the defects increase then the CV curve revealed humps which are an indication of Faradaic reaction. These results suggest that by the aid of defect centers and the morphology it is possible to predict the storage mechanism of the supercapacitor devices. This might be the first time that the defects, morphology, and the synergy of electrodes collectively show a control mechanism for EDLC and pseudosupercapacitor character. Such an interesting result should be further confirmed for other nanostructured ZnO morphologies such as nanodiscs, nanotetrapods, nanostars, nanoplates etc.

Acknowledgments:

This study is supported by a research grant from the Scientific and Technological Research Council of Turkey (TÜBİTAK, Grant No: 118C243) in the frame of 2232-International Fellowship for Outstanding Researchers. E. E. and F. B. thank TÜBİTAK for the financial support.

Conflict of interest:

There are no conflict of interest.

References

- [1] S. Najib, E. Erdem, Current progress achieved in novel materials for supercapacitor electrodes: Mini review, *Nanoscale Adv.* 1 (2019) 2817–2827.
- [2] S. Kasap, I.I. Kaya, S. Repp, E. Erdem, Superbat: Battery-like supercapacitor utilized by graphene foam and zinc oxide (ZnO) electrodes induced by structural defects, *Nanoscale Adv.* 1 (2019) 2586–2597.
- [3] S.K.S. Parashar, B.S. Murty, S. Repp, S. Weber, E. Erdem, Investigation of intrinsic defects in core-shell structured ZnO nanocrystals, *J. Appl. Phys.* 111 (2012) 113712.
- [4] H. Kaftelen, K. Ocakoglu, R. Thomann, S. Tu, S. Weber, E. Erdem, EPR and photoluminescence spectroscopy studies on the defect structure of ZnO nanocrystals, *Phys. Rev. B* 86 (2012) 14113.

- [5] E. Erdem, Microwave power, temperature, atmospheric and light dependence of intrinsic defects in ZnO nanoparticles: A study of electron paramagnetic resonance (EPR) spectroscopy, *Journal of Alloys and Compounds* 605 (2014) 34–44.
- [6] S. Repp, S. Weber, E. Erdem, Defect Evolution of Nonstoichiometric ZnO Quantum Dots, *J. Phys. Chem. C* 120 (43) (2016) 25124–25130.
- [7] P. Jakes, E. Erdem, Finite size effects in ZnO nanoparticles: An electron paramagnetic resonance (EPR) analysis, *Phys. Status Solidi RRL* 5 (2011) 56–58.
- [8] A. K. Srivastava, M. Deepa, K. N. Sood, E. Erdem, R. A. Eiche, Shape Selective Growth Of ZnO Nanostructures: Spectral And Electrochemical Response, *AML* 2 (2011) 142–147.
- [9] A. Burke, Z. Liu, H. Zhao, Present and future applications of supercapacitors in electric and hybrid vehicles, in: 2014 IEEE International Electric Vehicle Conference (IEVC): 17 - 19 Dec. 2014, Florence, Italy, Florence, IEEE, Piscataway, NJ, 2014, pp. 1–8.
- [10] T. Shimizu, C. Underwood, Super-capacitor energy storage for micro-satellites: Feasibility and potential mission applications, *Acta Astronautica* 85 (2013) 138–154.
- [11] F.S. Husairi, S.M. Ali, A. Azlinda, M. Rusop, S. Abdullah, Special Effect of Urea as a Stabilizer in Thermal Immersion Method to Synthesis Porous Zinc Oxide Nanostructures, *Journal of Nanomaterials* 2013 (2013) 1–7.
- [12] K. Kakiuchi, E. Hosono, T. Kimura, H. Imai, S. Fujihara, Fabrication of mesoporous ZnO nanosheets from precursor templates grown in aqueous solutions, *J Sol-Gel Sci Technol* 39 (2006) 63–72.
- [13] X. Wen, W. Wu, Y. Ding, Z.L. Wang, Seedless synthesis of patterned ZnO nanowire arrays on metal thin films (Au, Ag, Cu, Sn) and their application for flexible electromechanical sensing, *Journal of Materials Chemistry* 22 (2012) 9469.
- [14] J. Ungula, B.F. Dejene, H.C. Swart, Effect of annealing on the structural, morphological and optical properties of Ga-doped ZnO nanoparticles by reflux precipitation method, *Results in Physics* 7 (2017) 2022–2027.
- [15] M. Tuncer, F. Bakan, H. Gocmez, E. Erdem, Capacitive behaviour of nanocrystalline octacalcium phosphate (OCP) ($\text{Ca}_8\text{H}_2(\text{PO}_4)_6 \cdot 5\text{H}_2\text{O}$) as an electrode material for supercapacitors: Biosupercaps, *Nanoscale* 11 (2019) 18375–18381.
- [16] R. Genc, M.O. Alas, E. Harputlu, S. Repp, N. Kremer, M. Castellano, S.G. Colak, K. Ocakoglu, E. Erdem, High-Capacitance Hybrid Supercapacitor Based on Multi-Colored Fluorescent Carbon-Dots, *Sci. Rep.* 7 (2017) 11222.
- [17] M.Ö. Alaş, A. Güngör, R. Genç, E. Erdem, Feeling the power: Robust supercapacitors from nanostructured conductive polymers fostered with Mn^{2+} and carbon dots, *Nanoscale* 11 (2019) 12804–12816.
- [18] M. Toufani, S. Kasap, A. Tufani, F. Bakan, S. Weber, E. Erdem, Synergy of nano-ZnO and 3D-graphene foam electrodes for asymmetric supercapacitor devices, *Nanoscale* 58 (2020) 1189.
- [19] N. Abdullayeva, C.T. Altaf, M. Mintas, A. Ozer, M. Sankir, H. Kurt, N.D. Sankir, Investigation of Strain Effects on Photoelectrochemical Performance of Flexible ZnO Electrodes, *Sci. Rep.* 9 (2019) 1289.
- [20] Q. Yu, C. Yu, J. Wang, F. Guo, S. Gao, S. Jiao, H. Li, X. Zhang, X. Wang, H. Gao, H. Yang, L. Zhao, Gas sensing properties of self-assembled ZnO nanotube bundles, *RSC Adv* 3 (2013) 16619.
- [21] M. Raja, N. Muthukumarasamy, D. Velauthapillai, R. Balasundaraprabhu, S. Agilan, T.S. Senthil, Studies on bundle like ZnO nanorods for solar cell applications, *Solar Energy* 106 (2014) 129–135.

- [22] V. Kumar, V. Kumar, S. Som, A. Yousif, N. Singh, O.M. Ntwaeaborwa, A. Kapoor, H.C. Swart, Effect of annealing on the structural, morphological and photoluminescence properties of ZnO thin films prepared by spin coating, *Journal of Colloid and Interface Science* 428 (2014) 8–15. View Article Online
DOI: 10.1039/D0NR03921G
- [23] M. Schumm, M. Koerdel, S. Müller, C. Ronning, E. Dynowska, Z. Gołacki, W. Szuszkiewicz, J. Geurts, Secondary phase segregation in heavily transition metal implanted ZnO, *J. Appl. Phys.* 105 (2009) 83525.
- [24] V. Russo, M. Ghidelli, P. Gondoni, C.S. Casari, A. Li Bassi, Multi-wavelength Raman scattering of nanostructured Al-doped zinc oxide, *J. Appl. Phys.* 115 (2014) 73508.
- [25] R. Zhang, P.-G. Yin, N. Wang, L. Guo, Photoluminescence and Raman scattering of ZnO nanorods, *Solid State Sciences* 11 (2009) 865–869.
- [26] R. Cuscó, E. Alarcón-Lladó, J. Ibáñez, L. Artús, J. Jiménez, B. Wang, M.J. Callahan, Temperature dependence of Raman scattering in ZnO, *Phys. Rev. B* 75 (2007) G3.
- [27] E.G. Barbagioanni, R. Reitano, G. Franzò, V. Strano, A. Terrasi, S. Mirabella, Radiative mechanism and surface modification of four visible deep level defect states in ZnO nanorods, *Nanoscale* 8 (2016) 995–1006.
- [28] J. Tauc, R. Grigorovici, A. Vancu, Optical Properties and Electronic Structure of Amorphous Germanium, *phys. stat. sol. (b)* 15 (1966) 627–637.
- [29] T. Ruf, S. Repp, J. Urban, R. Thomann, E. Erdem, Competing effects between intrinsic and extrinsic defects in pure and Mn-doped ZnO nanocrystals, *J. Nanopart. Res.* 18 (5) 1–11.
- [30] G.R. Eaton, S.S. Eaton, D.P. Barr, R.T. Weber, *Quantitative EPR: A Practitioners Guide*, 1st ed., Springer Verlag Wien, s.l., 2010.
- [31] A. Lund, E. Sagstuen, A. Sanderud, J. Maruani, Relaxation-time determination from continuous-microwave saturation of EPR spectra, *Radiat. Res.* 172 (2009) 753–760.
- [32] A.R. bin Mohd Yusoff, *Graphene-based Energy Devices*, Wiley-VCH Verlag GmbH & Co. KGaA, Weinheim, Germany, 2015.